

# JPEG QUANTIZED COEFFICIENT RECOVERY VIA DCT DOMAIN SPATIAL-FREQUENTIAL TRANSFORMER

Mingyu Ouyang<sup>1</sup> and Zhenzhong Chen<sup>1</sup>

<sup>1</sup>School of Remote Sensing and Information Engineering, Wuhan University

## ABSTRACT

JPEG compression adopts the quantization of Discrete Cosine Transform (DCT) coefficients for effective bit-rate reduction, whilst the quantization could lead to a significant loss of important image details. Recovering compressed JPEG images in the frequency domain has attracted more and more attention recently, in addition to numerous restoration approaches developed in the pixel domain. However, the current DCT domain methods typically suffer from limited effectiveness in handling a wide range of compression quality factors, or fall short in recovering sparse quantized coefficients and the components across different colorspace. To address these challenges, we propose a DCT domain spatial-frequency Transformer, named as DCTransformer. Specifically, a dual-branch architecture is designed to capture both spatial and frequency correlations within the collocated DCT coefficients. Moreover, we incorporate the operation of quantization matrix embedding, which effectively allows our single model to handle a wide range of quality factors, and a luminance-chrominance alignment head that produces a unified feature map to align different-sized luminance and chrominance components. Our proposed DCTransformer outperforms the current state-of-the-art JPEG artifact removal techniques, as demonstrated by our extensive experiments.

## 1 INTRODUCTION

Aiming at aggregating the information and reducing data size of digital images, the JPEG (Joint Photographic Experts Group) algorithm [1] stands out among a variety of image compression methods for its high compression ratio and minimal reduction in visual quality. The JPEG compression process first divides the image into  $8 \times 8$  blocks and applies Discrete Cosine Transform [2] (DCT) to each block (refer to Figure 1. (a)). The produced DCT coefficients are then divided by a quantization matrix and rounded to the nearest integer. In Figure 1, an example of the DCT coefficients is depicted that is been quantized and recovered through our model, together with corresponding images. Since the human eye is less sensitive to high-frequency details and chrominance variants, JPEG compression relies on quantization and chroma subsampling to balance the compression ratio and preserved visual quality. The quantized coefficients are subsequently entropy-coded and packed into a compact bitstream for efficient transmission or storage. These characteristics enable JPEG images to be widely used across various devices, establishing it as one of the most critical image formats. However, as a lossy compression method, JPEG compression introduces coding artifacts, such as blockiness resulting from dividing the image into blocks or ringing artifacts due to the degradation of high-frequency information (refer to Figure 1. (d)), which makes a negative impact on the subjective visual quality.

To improve the visual experience, the task of removing compression artifacts from the decoded JPEG images, also referred to as JPEG artifact removal, has received great interest. Many traditional approaches [3, 4, 5, 6, 7, 8] have been developed to estimate the lost information from prior modeling perspectives or manually design filters. Deep learning-based methods, espe-

cially convolutional neural networks (CNNs) based ones, have also been proposed for image denoising such as some revolutionary works [9, 10, 11] showed significant improvements. Although CNN-based methods have achieved remarkable progress compared with traditional methods [11, 10, 12, 13, 14, 15], it still suffers from some limitations like weak in modeling long-range dependencies.

In summary, existing JPEG artifact removal approaches suffer from the following limitations in the practical deployment: (1) Most of them train a specific model for each quality factor and are not able to handle a wide range of quality factors. Due to the flexibility of JPEG compression, varying quality factors degrade images differently in coefficient representations, posing challenges in recovering the identical original image. (2) In existing DCT coefficient recovery methods, luminance and chrominance components are processed separately due to further subsampling of chrominance components and different quantization values. (3) Very few studies consider directly learning from their decoded frequency coefficients, thus there would be some potential to further explore in the DCT domain.

To address the above limitations, we introduce a DCT domain spatial-frequency Transformer (DCTransformer) that employs a single frequency domain model to recover the JPEG quantized coefficients. Our core idea targets the lossy steps in JPEG compression and directly recovers coefficients within the DCT frequency domain. In particular, we present a dual-branch Spatial-Frequency Transformer Block (SFTB) for capturing correlations among both spatial and frequency dimensions of collocated DCT coefficients. Furthermore, by integrating quantization matrix embedding and a luminance-chrominance alignment head, our single model effectively handles the recovery of compressed luminance and chrominance components across a wide range of compression quality factors. Besides, different from prevalent CNN-based models in quantized coefficient recovery tasks, our approach employs a Transformer-based ar-

Corresponding author: Zhenzhong Chen, E-mail:zzchen@iee.org

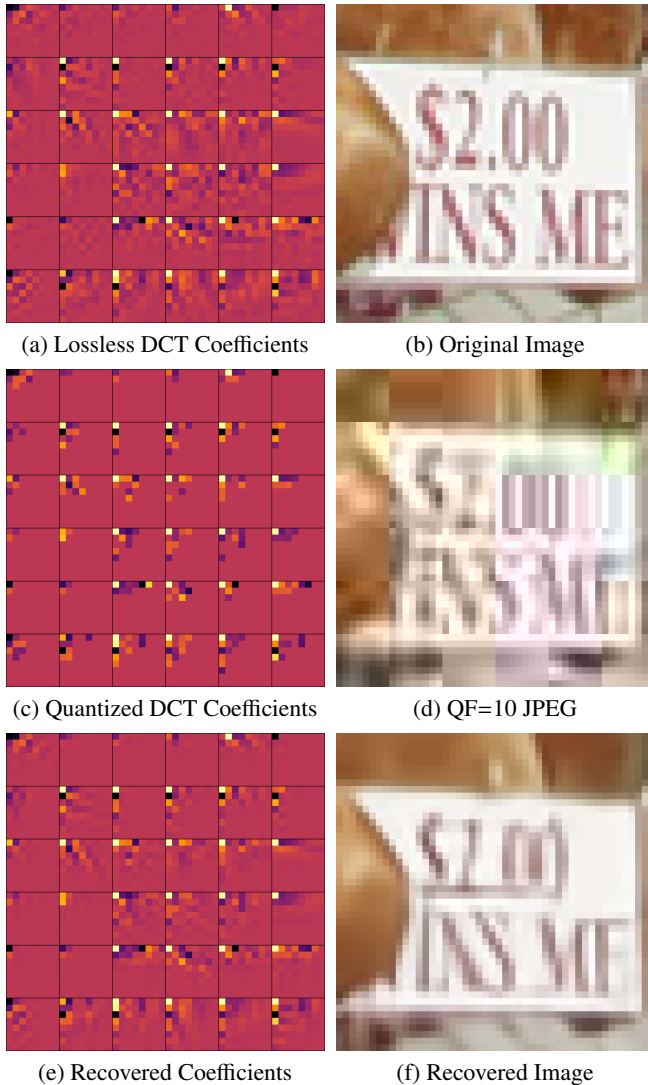


Figure 1: Visualizations of the quantization and recovery of DCT coefficients and corresponding images. (a)-(b) The original image and its lossless DCT coefficients. (c)-(d) Compressed JPEG at QF = 10 and its highly sparse quantized coefficients. (e)-(f) Recovered coefficients of our DCTransformer and the reconstructed image. Note that only the coefficients of the Y channel are presented.

chitecture in the DCT domain. To the best of our knowledge, it is the first time that a Transformer-based model is adopted for JPEG quantized coefficient recovery in the DCT domain.

In summary, the main contributions of this paper are as follows:

1. A DCT domain spatial-freqential Transformer for JPEG quantized coefficients recovery (DCTransformer) is proposed. The dual-branch self-attention architecture is specifically designed for capturing the correlations across different dimensions within collocated DCT coefficients. Additionally, the feature concatenation and residual connections facilitate handling the sparsity of quantized DCT coefficients.

2. Towards a single model handling luminance and chrominance components across a wide range of quality factors. By incorporating the quantization matrix embedding and a luminance-chrominance alignment head, we effectively introduce the information of the quantization matrix and unify different-sized components into our DCTransformer.
3. The proposed Transformer-based approach is fully based on learning in the DCT domain. To the best of our knowledge, this is the first research that adopts a Transformer-based model within the DCT domain to directly learn from JPEG quantized coefficients. We also provide a DCT domain quantitative evaluation for thorough analysis. Our DCTransformer achieves state-of-the-art performance in color JPEG restoration, among both the pixel and DCT domain approaches.

The remainder of this paper is structured as follows. Section II reviews the frequency domain learning and quantized coefficients recovery. The proposed DCT domain method is introduced in Section III. Experiments and ablation studies on benchmark datasets demonstrate the effectiveness of our proposed method in Section IV. Finally, Section V concludes our paper.

## 2 RELATED WORKS

Quantized coefficients recovery, aiming to improve the quality of compressed images, shares the same objective as JPEG artifact removal but directly processes decoded coefficients as input and output. Due to the quantized DCT coefficients having excessive invalid values, this problem is reflected in the loss of image details in the pixel domain. Traditional quantized coefficient recovery methods address the degradation problem by approximating the lost information via Gaussian [3] and Laplace distributions [4], or manually design a filter to reduce the artifact [5, 6, 8]. These estimation approaches deviate from the complexity in reality practice, which leads to critical limitations of the performance. Given the powerful nonlinear mapping capability shown in various vision tasks, deep neural networks [10, 11] have been introduced to restore compressed JPEG images. However, implementing a model trained for each quality factor is unrealistic. To handle the varying quality factors, which are unknown since they are not stored alongside the JPEG, [16] attempts to incorporate the quantization matrix by concatenating it with images as additional input channels, achieving state-of-the-art performance. [15] directly predicts the quality factor from the lossy image, and reconstructs the image by embedding the adjustable quality factor to achieve flexibility. Most recently, [17] presents an unsupervised learning strategy for compression quality estimation by contrastive learning. [18] proposes a variational inference framework that could be used for JPEG compression artifacts reduction.

Despite these existing methods operating in the frequency domain, such as QGAC, our method differs in three main aspects. Firstly, while traditional methods typically apply a CNN-based model, we propose a Transformer-based approach for this task. Secondly, some methods such as QGAC employ a convolutional filter manifold to introduce the quantization matrix to guide the recovery. Yet we find that our quantization matrix embedding can efficiently and directly introduce varying loss information

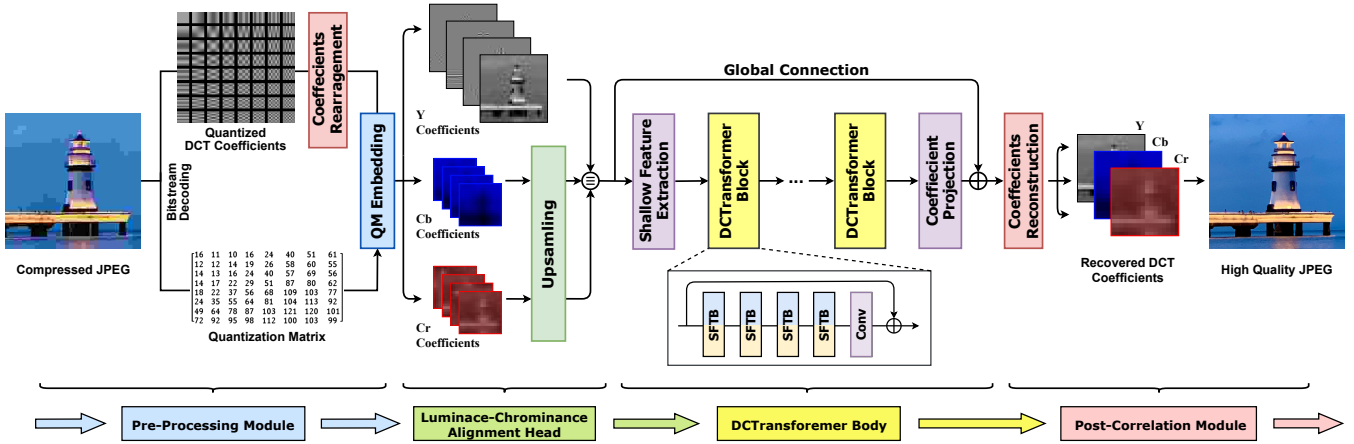


Figure 2: An overview of the pipeline of the proposed DCTransformer for JPEG quantized coefficient recovery. DCTransformer consists of four modules, *i.e.*, pre-processing module, luminance-chrominance alignment head, DCTransformer body, and post-correlation module. The pre-processing module includes operations of quantization matrix embedding and coefficient rearrangement to prepare collocated DCT coefficients. Then the luminance-chrominance alignment head unifies different-sized Y and CbCr coefficients and fed into the DCTransformer body. This is processed through several Spatial-Frequency Transformer Blocks (SFTB) in the DCTransformer body. Finally, the post-correlation module reconstructs the full image from the recovered coefficients.

from quantization, whilst reducing the computational cost of the network. Thirdly, in existing methods, the recovery of color JPEG is divided into two stages, first restoring the Y channel as intermediate output, and then separately restoring the Cb and Cr channels. In contrast, our method provides an alignment of the unified feature map to simultaneously recover both the luminance and chrominance components.

### 3 THE PROPOSED METHOD

Given an original image  $I_{gt}$  and the corresponding JPEG compressed image  $I_j$ , the JPEG compression process can be formulated as:

$$C_j = \text{round}(Q(D(I_{gt}))) + e, \quad (1)$$

where  $C_j$  is the quantized DCT coefficients of  $I_j$ ,  $D(\cdot)$  is the DCT operation,  $Q(\cdot)$  denotes quantization controlled by the quantization matrix (QM), and  $e$  encapsulates other compression losses, *i.e.*, chroma subsampling. Thus, we can thus formulate the task of JPEG quantized coefficient recovery as:

$$I_{rec} = D^{-1}(Q^{-1}(C_j)), \quad (2)$$

where  $D^{-1}(\cdot)$  and  $Q^{-1}(\cdot)$  denote inverse DCT and inverse quantization operations respectively, and  $I_{rec}$  is the recovered image. Our primary objective is to design an optimal function for  $Q^{-1}(\cdot)$  that minimizes the distance between  $I_{gt}$  and  $I_{rec}$ , *i.e.*,  $\|I_{gt} - I_{rec}\|$ , under constraints of recovering the coefficients in DCT domain.

Note that finding  $Q^{-1}(\cdot)$  is an ill-posed problem due to the lossy nature of the rounding and downsampling operation, which makes the inverse quantization process nontrivial. The recovery of quantized coefficients is not merely a mathematical inversion problem, but also a perceptual one as it should aim to maximize the perceived quality of the recovered image. This necessitates our employment of a learning-based approach that can incorporate perceptual capabilities into the recovery.

#### 3.1 The Overall Framework

We propose a novel framework aiming at recovering the quantized coefficients in the DCT domain. Figure 2 shows an overview of our framework (note that some components are omitted for simplicity), which consists of four modules as follows.

The first module, a coefficient pre-processing module, is designed to enable the single model to recover JPEG compressed images with varying quality factors. It consists of a quantization matrix (QM) embedding and a coefficient rearrangement operation. The second module, a luminance-chrominance alignment head, allows the model to simultaneously process luminance and chrominance components, with producing a unified feature map. The third module, which serves as the core structure for quantized coefficient recovery, employs a DCT domain spatial-frequency Transformer network, named as DCTransformer. DCTransformer consists of a shallow feature extraction layer, several DCTransformer blocks, a coefficient projection layer, and a global connection. Each DCTransformer block contains several Spatial-Frequency Transformer Blocks (SFTBs) and a convolutional layer, followed by a residual connection. The last module is a post-correlation module that incorporates coefficient reconstruction and inverse DCT operation, converting the recovered quantized DCT coefficients into restored pixel domain images.

#### 3.2 QM Embedding and DCT Coefficient Rearrangement

Many frequency domain methods are suffering from different compression quality factors since they bring differences in frequency domain representations. Thus many previous models are trained for a specific quality factor or channel component. Otherwise, the quantization matrix is regarded as the input to the network for spatial feature extraction or predicted from the unknown to approximate the loss of information. To address these problems, we perform the operations of 1) *quantization matrix*

embedding and 2) DCT coefficient rearrangement in our pre-processing module. A schematic diagram of these operations is shown in Figure 3.

1) *Quantization Matrix Embedding*: For JPEG compression without lossy downsampling operation, the losses are all caused by quantization. Considering  $B_{coef}$  in each of the  $8 \times 8$  coefficients block and corresponding quantization matrix  $Q_{mat}$ , the loss  $\delta_{coef}$  can be expressed as:

$$\delta_{coef} = \text{round}\left(\frac{B_{coef}}{Q_{mat}}\right) - \text{round}\left(\frac{B_{coef}}{Q_{mat}}\right) \cdot Q_{mat}, \quad (3)$$

where *round* is a function that rounds to the nearest integer, and the division is element-wise. This operation restricts the coefficient loss to the loss range of the rounding operation, which signifies the quantization value for the corresponding frequency in the quantization matrix. Derived from Eq. (3), the loss  $\delta_{coef}$  is satisfies:

$$\delta_{coef} = \theta_i \odot Q_{mat}, \quad (4)$$

where  $\odot$  donates Hadamard product of two  $8 \times 8$  matrix and  $\theta$  is a relative factor in range:

$$-0.5 < \theta < 0.5 \quad \forall \theta_i \in \theta. \quad (5)$$

Inspired by this, we propose an intuitive approach as quantization matrix embedding. Recall that previous methods, like [14] employs convolutional layers to extract features from the quantization matrix, or [16] duplicates the quantization matrix and concatenate them with images as additional input channels. We suggest they may have drawbacks since the information of the quantization matrix should be combined with DCT coefficients that are quantized by it. Therefore, we recover the direct representation of quantization losses, as in the JPEG decoding process, the lossy coefficients are block-wise multiplied by the quantization matrix, resulting in the value range from -1024 to 1023 approximately. The proposed quantization matrix embedding can be formulated as:

$$\tilde{B}_{coef} = B_{coef} \odot Q_{mat}, \quad (6)$$

where  $Q_{mat}$  is the quantization matrix. This is illustrated in Figure 3. a), b). Hence, the loss of  $\tilde{B}_{coef}$  in position  $i, j \in N^{(0, \dots, 7)}$  can be constrained by the value of the quantization matrix at position  $(i, j)$ :

$$-0.5 * Q_{mat}(i, j) < \tilde{\delta}_{coef}(i, j) < 0.5 * Q_{mat}(i, j). \quad (7)$$

2) *DCT Coefficient Rearrangement*: Due to the  $8 \times 8$  block-based DCT operation in JPEG compression, each  $8 \times 8$  block contains 64 different frequency components of the original pixel domain image. To emphasize the spatial and frequential correlations within coefficients, we rearrange the embedded DCT coefficients into collocated DCT maps. For each YCbCr channel, we reshape the coefficients from the shape  $1 \times H \times W$  to  $64 \times \frac{H}{8} \times \frac{W}{8}$ , where the 64 represents different frequency components, and the  $H$  and  $W$  denote the original height and width of the Y or CbCr channel, respectively.

To better understand the collocated DCT coefficients, we illustrate them from the spatial  $(x, y)$  and frequential  $(\lambda)$  axes, as shown in Figure 3. c). Most importantly, after the rearrangement, the DCT coefficients are collocated with spatial features. Analyzing along the frequential (first) dimension, 64 frequency

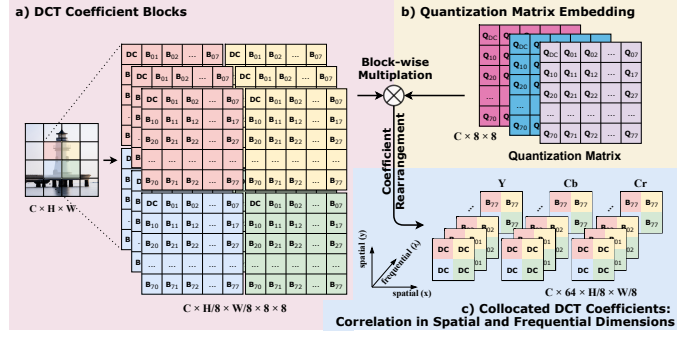


Figure 3: The schematic illustrations of a) Decoded DCT coefficient blocks. b) The proposed quantization matrix embedding. c) The rearrangement of collocated DCT coefficients. The resulting collocated DCT coefficients have an intrinsic correlation in both spatial and frequential dimensions.

components within the same  $8 \times 8$  block are represented by different channels at the same spatial position. Meanwhile, along the spatial (last two) dimensions, adjacent spatial positions correspond to the same frequency components in neighboring  $8 \times 8$  blocks. This forms the basic shape of the input and output feature map for our frequential-spatial feature extraction approach.

### 3.3 Luminance-Chrominance Alignment Head

Color JPEG images encode information in YCbCr colorspace. To achieve higher compression performance, the Cb and Cr channels, also known as chrominance components, are quantized to carry less information and subsampled to half-sized. Due to the high sensitivity of prior frequency domain models, the correction process for color JPEG images in [19, 14] recovers the luminance and chrominance coefficients through separate models or different stages. These may reduce efficiency and lead to insufficient information interaction between the luminance and chrominance components.

To manage different-sized Y and CbCr components, we propose a luminance-chrominance alignment head for color JPEG coefficients recovery. It takes in DCT collocated coefficients from both luminance  $X_y$ , and chrominance components  $X_{cb}$  and  $X_{cr}$  as input, produces an aligned and unified DCT feature map  $X_{aligned}$  feeding to the DCTransformer body. In detail,  $X_y$ ,  $X_{cb}$ , and  $X_{cr}$  are first projected into higher dimensions by three different convolutional layers, respectively. Subsequently,  $X_{cb}$  and  $X_{cr}$  are upsampled twice by each of the two transpose convolutional layers to match the size of  $X_y$ . Finally, we channel-wise concatenate the three and use a  $3 \times 3$  convolutional layer  $H_{cat}(\cdot)$  to fusion the components.

$$X_{aligned} = H_{cat}([H_y(X_y), H_{cb}(X_{cb}), H_{cr}(X_{cr})]), \quad (8)$$

where  $[\cdot]$  represents the concatenation operation,  $H_y$ ,  $H_{cb}$  and  $H_{cr}$  stand for convolutional heads for each component. This alignment ensures the luminance and chrominance coefficients are spatially matched and mapped to higher dimensional feature space for the following feature extraction.

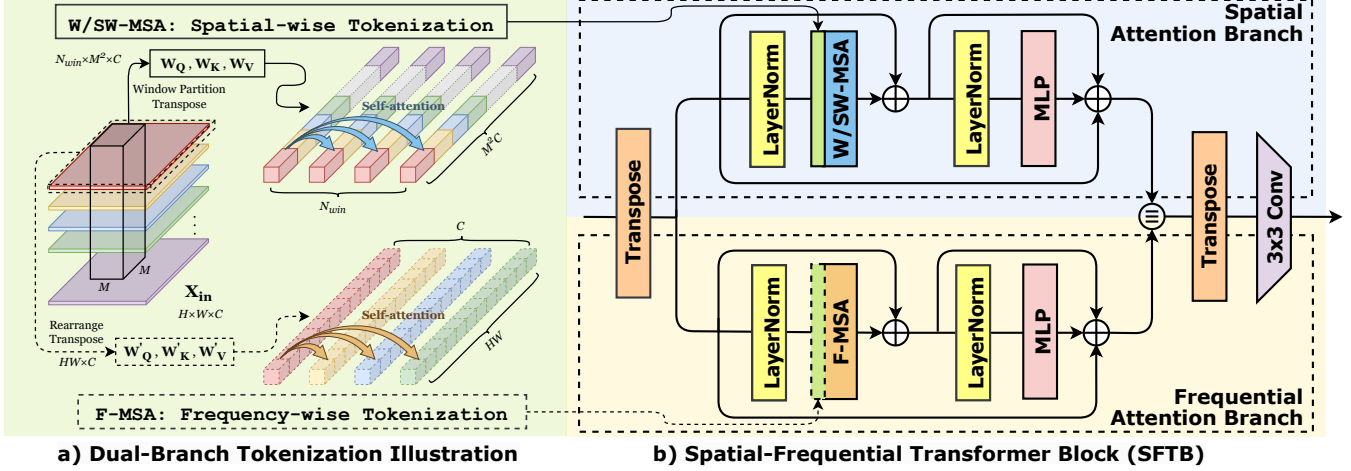


Figure 4: The architecture of our Spatial-Frequency Transformer Block (SFTB). a) Illustration of the tokenization in spatial-wise and frequency-wise self-attention to extract diverse correlations. Note that multi-head design and learnable biases have been omitted for simplicity. b) The dual-branch architecture of SFTB. Each SFTB consists of two attention branches: spatial attention branch and frequential attention branch. The outputs of two branches are then channel concatenated and passed through a  $3 \times 3$  convolutional layer.

### 3.4 DCTransformer Body

1) *Dual-branch Spatial-frequential Transformer Architecture:* The Transformer [20] and its self-attention module are primarily designed for sequence modeling and extracting correlations within long-range dependencies. It also shows promising results when adapted to computer vision tasks [21, 22, 23] compared to convolution-based methods. However, the quantization operation produces many invalid coefficients to shorten the coding, resulting in spatially sparse where coefficients are quantized to zeros, especially more significant for the high-frequency components [24]. Because of this sparsity, the representation of DCT coefficients is relatively unsuitable for CNNs to extract localized spatial features or insufficient for standard Transformers to compute the attention along the patches.

After the coefficient rearrangement, the intrinsic spatial and frequential correlations of collocated quantized DCT coefficients manifest in different dimensions, as shown in Figure 3. c). Aiming at extracting these correlations for the recovery, we introduce a DCT domain frequential-spatial Transformer architecture, namely DCTransformer, which serves as the core module for quantized coefficient recovery. Specifically, the dual-branch design of our DCTransformer is intended to capture correlations across both spatial and frequential dimensions.

An illustration of the dual-branch spatial-frequential self-attention structure is shown in Figure 4. To be specific, in the DCTransformer block, the input feature map  $X_{in}$  is evenly copied into  $X_{spat}$  and  $X_{freq}$  undergoes two parallel branches, named spatial attention branch and frequential attention branch, each involving a different type of rearrangement and self-attention mechanism. These operations can be represented as:

$$\begin{aligned} X_{spat}, X_{freq} &= X_{in}, \\ Y_{spat}, Y_{freq} &= B_{spat}(X_{spat}), B_{freq}(X_{freq}), \end{aligned} \quad (9)$$

where  $Y_{spat}$  and  $Y_{freq}$  are output feature maps of the spatial attention branch  $B_{spat}$  and frequential attention branch  $B_{freq}$ , respectively.

2) *Spatial Attention Branch:* For the spatial branch in our SFTB, we utilize a Swin Transformer Block [22] to extract spatial correlations in collocated DCT coefficients. Note that this operation is still fully in the DCT domain, where we extract the spatial correlation within the rearranged DCT coefficients. Swin Transformer, with a modification of the standard multi-head self-attention (MSA), computes local attention within each partitioned window, thereby generally reducing computational complexity. Figure. 4 shows a simplified version of this mechanism. The window self-attention (W-MSA) and shifted window self-attention (SW-MSA) are alternatively ordered in successive SFTBs. Moreover, the cross-window connections are facilitated by the shifting window operation. As illustrated in Figure 4. (b), the spatial attention branch consists of one W/SW-MSA module and a multiple-layer perception (MLP), accompanied by two layer normalizations (LN) preceding each SW-MSA and MLP.

In detail, the input is first partitioned into  $M \times M$  non-overlapped windows to compute the self-attention. Given an input feature map as  $H \times W \times C$ , the partitioned windows are reshaped to  $\frac{HW}{M^2} \times M^2 \times C$ , where standard self-attention is computed in each shaped  $M^2 \times C$  window. The entire process of the spatial attention branch is expressed as follows:

$$\begin{aligned} X'_{spat} &= \text{W/SW-MSA}(\text{LN}(X_{spat})) + X_{spat}, \\ Y_{spat} &= \text{MLP}(\text{LN}(X'_{spat})) + X'_{spat}, \end{aligned} \quad (10)$$

where the W/SW-MSA donates the operation of window-based multi-head self-attention and shifted window-based multi-head self-attention; MLP regards two successive multiple layer perceptions, projecting the embedded feature into a higher dimensional space representation, supplemented with a GELU function to introduce more non-linearity.

3) *Frequential Attention Branch:* Collocated DCT coefficients are rearranged into spatially aligned, with each of 64 frequency components in 64 separate channels. To emphasize extracting the dependencies in different frequency components in the frequential attention branch, we propose a frequency multi-head

self-attention (F-MSA), in which each channel of the frequency feature map is process isolated as a token. In this approach, the attention is performed on the channel level so that the information within each frequency can interact globally with each other. Different from directly projecting each patch of the feature map as  $Q$ ,  $K$ , and  $V$ , the input  $X_{freq}$  is firstly reshaped into  $HW \times C$ , and linear projected through  $W_Q$ ,  $W_K$ , and  $W_V$  into  $Q$ ,  $K$ , and  $V$  as  $C$  tokens in shape  $HW \times 1$ . In order to attend more frequency patterns, we extend it to multi-heads by splitting  $Q$ ,  $K$ , and  $V$  into  $N = \frac{C}{d_{head}}$  heads in parallel, where in our experiments  $d_{head}$  is set to 32. Subsequently, the standard attention mechanism is computed within each frequency-wise token, and outputs from all heads are concatenated. We illustrate this modified tokenization process of F-MSA in Figure 4 (a). The entire frequential branch can be formulated as:

$$\begin{aligned} X'_{freq} &= \text{F-MSA}(\text{LN}(X_{freq})) + X_{freq}, \\ Y_{freq} &= \text{MLP}(\text{LN}(X'_{freq})) + X'_{freq}, \end{aligned} \quad (11)$$

where the F-MSA donates frequential multi-head self-attention; MLP has the same structure as the spatial branch and consists of two successive multiple-layer perceptions and a GELU function.

Note that within the F-MSA operation, we utilize two  $3 \times 3$  depth-wise convolutional layers with a GELU activation in the middle as a channel-wise positional embedding. Each channel is added by a  $X_{ebd}$  feature map before projecting into  $Q$ ,  $K$ , and  $V$ . Since [25] has shown the potential of learnable positional embedding, this could enable attention heads to exploit the channel-wise information of different frequencies.

**4) Feature Concatenation in SFTB and Building DCTransformer Block:** Low quality factors correspond to higher values in the quantization matrix, which bring many zeros (e.g. approximately 95% are zeros at QF=10, approximately 90% are zeros at QF=20) in quantized coefficients, especially more obvious for high frequencies. Due to so many invalid tokens generated by this sparsity, we apply the feature concatenation to fusion the feature maps from two branches in SFTB. Consider  $Y_{spat}$  and  $Y_{freq}$  are the output feature maps of two branches. Instead of adding them together as  $Y_{spat} + Y_{freq}$ , we concatenate them along the channel dimension as  $[Y_{spat}, Y_{freq}]$  and pass through a convolution operation. Moreover, we incorporate residual connections [26] in each branch to further alleviate the sparse input problem. We can formulate the combined operations as:

$$Z_{out} = H_{\text{CONV}}([Y_{spat} + X_{spat}, Y_{freq} + X_{freq}]), \quad (12)$$

where  $Z_{out}$  is the output feature map,  $H_{\text{CONV}}(\cdot)$  is the  $3 \times 3$  convolutional layer in SFTB,  $X_{spat}$ ,  $X_{freq}$  /  $Y_{spat}$ ,  $Y_{freq}$  are the input/output feature maps of the two branches. This helps both reserve the previous information and avoid too much invalid information. Moreover, utilizing a  $3 \times 3$  convolution contributes to the integration of local neighboring information in two branches. Replacing adding function with feature concatenation followed by convolution leads to obviously superior results, as verified in Section IV-D of our ablation studies.

As shown in Figure 2, DCTransformer is comprised of a series of stacked DCTransformer blocks. Each DCTransformer block is a residual block with several RSTBs and a convolutional layer before the residual connection. Given intermediate features  $F_1, F_2, \dots, F_K$  in the  $i$ -th DCTransformer Block, the entire DCTransformer Block with  $K$  SFTBs can be expressed

as:

$$\begin{aligned} F_{i,j} &= \text{SFTB}_{i,j}(F_{i,j-1}), \quad j = 1, 2, \dots, K, \\ F_{out,i} &= H_{\text{CONV}_i}(F_{i,K}) + F_{i,1}, \end{aligned} \quad (13)$$

where  $H_{\text{CONV}}(\cdot)$  is the  $3 \times 3$  convolutional layer in the SFTB. Using such a convolutional layer followed by Transformer-based feature extraction can introduce the translational equivalence of the convolution operation. This composition design takes advantage of the strengths of residual learning [26], also providing more aggregation of features at different stages in the network.

### 3.5 Dual-domain Loss Function

To align the optimization objective of our DCT domain model with the pixel domain to reach a better visual effect, we propose a dual-domain loss to balance the quality between pixel and frequency domains. Either a single pixel domain loss or a frequency domain loss usually leads to worse results, as verified in Section IV-D. For the pixel domain, we utilize the Charbonnier loss [27] expressed as:

$$L_{\text{pixel}} = \sqrt{\|\mathcal{F}(x) - \mathcal{F}(\hat{x})\|^2 + \epsilon^2}, \quad (14)$$

where  $\mathcal{F}(\cdot)$  represents reconstruction operation, converting the lossless coefficients  $x$  and recovered coefficients  $\hat{x}$  to the pixel domain images, and  $\epsilon$  is a constant value set to  $10^{-3}$  empirically. For recovered DCT coefficients in the frequency domain, we adopt the same L1 loss as [19], which is:

$$L_{\text{freq}} = \|x - \hat{x}\|_1. \quad (15)$$

To sum both up, the proposed dual-domain loss function is defined as:

$$L_{\text{dual}} = L_{\text{freq}} + \lambda L_{\text{pixel}}, \quad (16)$$

where the  $\lambda$  donates a balancing ratio considering the different value ranges, which is set as 255 for our experiment.

## 4 EXPERIMENTS

### 4.1 Implement Details

**Dataset Preparation.** For the training stage, we use DIV2K and Flickr2k [28] as training sets, which contain 800 and 2650 high-quality images. For experimental evaluation, we use LIVE1 [29] [30], Classic-5 [31], BSDS500 [32], Urban100 [33] and 8-bit ICB [34] datasets. For grayscale experiments, we first convert color images from RGB into YCbCr colorspace, then we use the Y channel for the grayscale JPEG recovery.

**Training Settings.** We use the Adam[35] optimizer with default parameters  $\beta_1 = 0.9$  and  $\beta_2 = 0.99$  during all training procedures. Since the input sent to the network is filled with a large part of zeros, we adopt gradient clipping with a maximum value of 0.2 to stabilize the training procedure. The learning rate is set at  $1 \times 10^{-4}$  from the start, and gradually rises to  $4 \times 10^{-4}$  in the first quarter of epochs. Then we apply a cosine annealing decay strategy[36], decreasing the learning rate to  $1 \times 10^{-5}$ . The batch size is set to 96. We implement our model on the PyTorch 1.7.1 framework [37], and train all models on six NVIDIA 3090 GPUs.

During training procedures, we generate quantized/lossless coefficients as training pairs from high-quality images. We first

Table 1: Pixel domain evaluation on **Color** JPEG Images from Three Benchmark Datasets. Represented in **PSNR(dB)/SSIM/PSNR-B(dB)** Format. The Best and Second Best Performances are **Boldfaced** and Underlined, Respectively. Please Note that Marker \* Represents DCT Domain Methods.

Dataset	QF	JPEG	QGCN[16]	FBCNN[15]	ARCRL[17]		QGAC*[14]	DCTransformer*
LIVE1	10	25.69/0.743/24.20	27.78/0.804/27.55	27.77/0.803/27.51	27.80/0.805/27.57		27.62/0.804/27.43	<b>28.06/0.808/27.87</b>
	20	28.06/0.826/26.49	30.12/0.870/29.74	30.11/0.868/29.70	30.23/0.872/29.85		29.88/0.868/29.56	<b>30.32/0.873/30.00</b>
	30	29.37/0.861/27.84	31.44/0.898/30.97	31.43/0.897/30.92	31.58/ <b>0.900</b> /31.13		31.17/0.896/30.77	<b>31.62/0.900/31.23</b>
	40	30.28/0.882/28.84	32.33/0.914/31.83	32.34/0.913/31.80	<b>32.53/0.916</b> /32.04		32.05/0.912/31.61	<u>32.51/0.916/32.07</u>
BSDS500	10	25.84/0.741/24.13	27.85/0.800/27.53	27.85/0.799/27.52	27.91/0.803/27.59		27.74/0.802/27.47	<b>27.95/0.803/27.87</b>
	20	28.21/0.827/26.37	30.18/0.870/29.61	30.14/0.867/29.56	<b>30.31/0.872</b> /29.74		30.01/0.869/29.53	30.21/0.871/30.07
	30	29.57/0.865/27.72	31.52/0.899/30.79	31.45/0.897/30.72	<b>31.69/0.901</b> /30.96		31.33/0.898/30.70	31.54/ <b>0.901</b> /31.34
	40	30.52/0.887/28.69	32.44/0.916/31.62	32.36/0.913/31.52	<b>32.66/0.918</b> /31.82		32.25/0.915/31.50	<u>32.46/0.917/32.21</u>
ICB	10	29.44/0.757/28.53	32.00/0.813/31.96	<u>32.18/0.815</u> /32.15	32.05/0.813/32.04		32.06/ <u>0.816</u> /32.04	<b>32.73/0.818/32.69</b>
	20	32.01/0.806/31.11	34.21/0.842/34.15	<u>34.38/0.844</u> /34.34	34.32/0.842/34.31		34.13/0.843/34.10	<b>34.70/0.843/32.64</b>
	30	33.20/0.831/32.35	35.22/0.856/35.15	<u>35.41/0.857</u> /35.35	35.37/0.856/35.35		35.07/ <b>0.857</b> /35.02	<b>35.61/0.857/35.54</b>
	40	33.95/0.840/33.14	35.78/0.860/35.71	<u>36.02/0.866</u> /35.95	35.99/0.860/35.97		35.71/0.862/35.65	<b>36.14/0.866/36.05</b>

randomly crop the patches with the size  $256 \times 256$  pixels, then encode these cropped patches into JPEG images at quality factors from 10 to 80, with a step size of 10. Random rotation and flipping are applied as augmentation methods. The encoding and decoding processes are facilitated by the OpenCV library[38], which internally leverages the libjpeg by Independent JPEG Group [39] for efficient JPEG data handling. Since our method processes images entirely in the DCT domain, we use `torchjpeg.codec.read_coefficients` [14] to decode the quantized DCT coefficients and quantization matrix from compressed JPEG images.

## 4.2 Pixel Domain Evaluation

### 1) Performance on color JPEG quantized coefficients recovery.

We compare the proposed method with other state-of-the-art methods for JPEG quantized coefficients recovery on three common test datasets LIVE1, Urban100, BSDS500, and Kodak. We calculate the PSNR, SSIM [40], and PSNR-B [41] for pixel domain evaluation. The quantitative results are reported in Table 1. To emphasize the concept of frequency domain learning, we use marker \* to refer to methods of recovering the quantization coefficients in the DCT domain. Note that all the results of our DCTransformer are predicted from the single model. Besides, the marker ' specifies the method of training each model for a specific quality factor. As can be seen from Table 1, our method has significantly better results than the state-of-the-art DCT domain method and moderately better results than FBCNN[15] and ARCRL[17], which are the state-of-the-art methods in the pixel domain. It is worth mentioning that our model only has 21.1 M parameters, while FBCNN has 65.7M and QGAC has 259.4M parameters. This indicates that our architecture is efficient in learning feature representations for restoration in the DCT domain, and has the potential for further improvement. Of particular note, our deblocking results are substantially superior on the PSNR-B metric, which suggests our effectiveness in eliminating the artifacts and blockiness. We also provide a subjective comparison of the recovered images of "buildings.bmp" from the LIVE1 dataset. As presented in Figure 5, our model can alleviate the visual artifacts and restore richer high-frequency

textures, *i.e.* on the shutter and the rooftop, while other methods suffer from over-smoothness and their recovered images have less natural details.

Figure 6 presents another comparison of the results for artifact removal. The channel residual refers to the difference between the recovered images and the corresponding ground truth. We convert the recovered results to YCbCr colorspace and present the residual of each channel separately. Through this example, we highlight that the proposed DCT domain method is able to handle color components quite well. It is worth emphasizing that since our method generates upsampled chrominance components in the DCT domain, the recovery result from our method shows a more consistent color with the ground truth, *i.e.* less red-colored blurring in the area of the sky. That also demonstrates the design of luminance-chrominance alignment has an advantage in eliminating large area color artifacts, which eventually produces a more visually pleasing restoration.

### 2) Performance on grayscale JPEG quantized coefficients recovery.

We also trained our model with the acceptance of only Y coefficients for grayscale JPEG recovery. The luminance-chrominance alignment head is replaced by convolutional layers in our DCTransformer for grayscale experiments, with other settings remaining unchanged. Table 2 reports the PSNR, SSIM, and PSNR-B results on the Classic-5, LIVE1, and BSDS500. Although our model is designed for recovering both the luminance and chrominance components, we can also match the previous state-of-the-art grayscale correlation models, and consistently provides high PSNR-B results demonstrating our strength in removing blockiness.

### 3) Generalization capabilities at a wide range of quality factors.

Since the quality factor is flexible but unknown for JPEG compressed images, generalizing a robust method in the recovery can avoid assembling quality-specific trained models. As one of the main superiority of our approach, the generalization capabilities enable our model to handle a wide range of compression quality factors, which allows our model to be more practical. To present this feature, we first show the qualitative results of two recovered images from the LIVE1 dataset in Figure 7. The

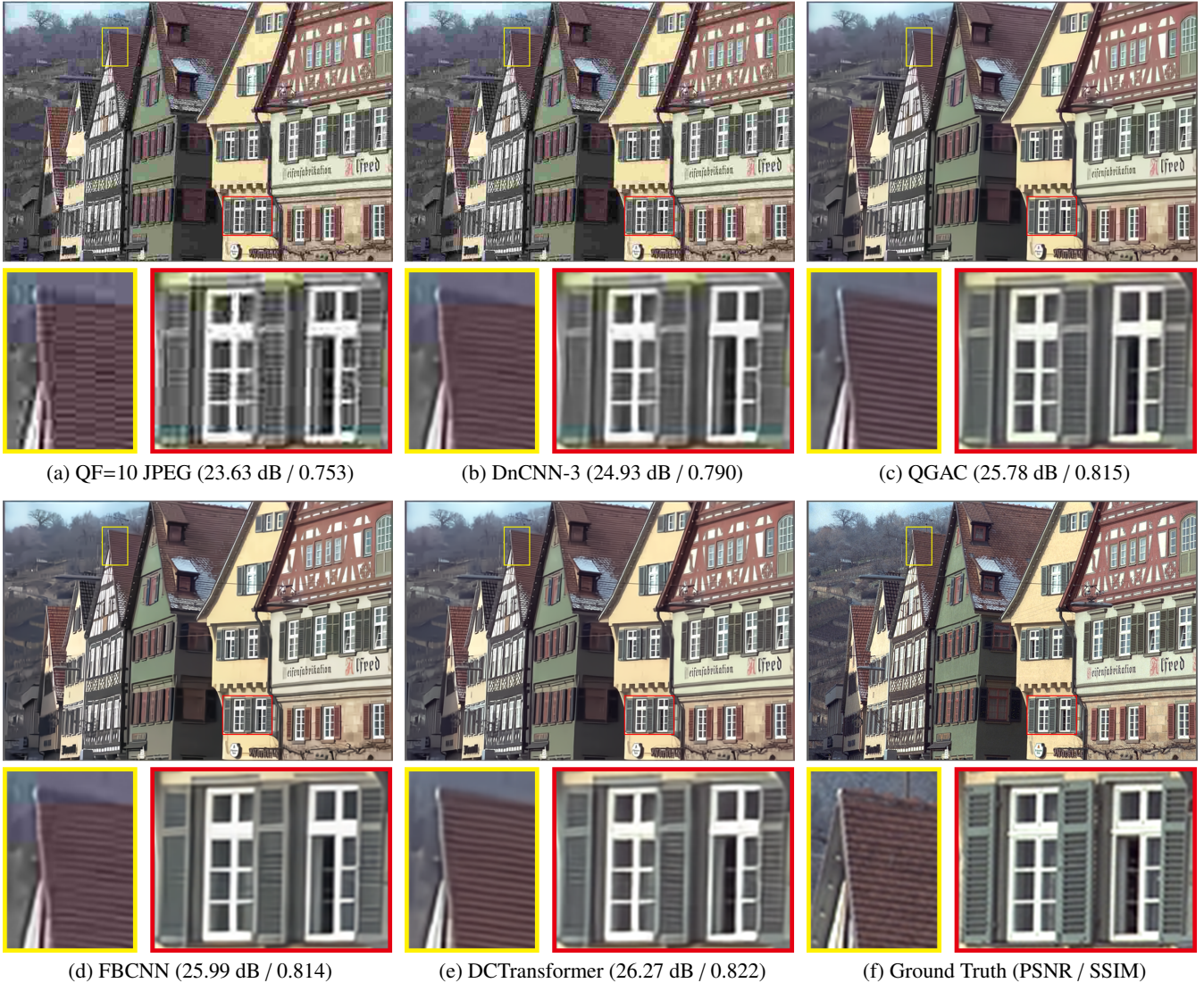


Figure 5: Recovery comparisons of "LIVE1: buildings.bmp" with JPEG compression quality factor = 10. (a) compressed JPEG in 23.63 dB and SSIM 0.790. (b) DnCNN-3 [10] in 24.93 dB and SSIM 0.753. (c) QGAC [14] method in 25.78 dB and SSIM 0.815. (d) FBCNN [15] method in 25.99 dB and SSIM 0.814. (e) our DCTransformer in 26.23 dB and SSIM 0.820. (f) the original image. Note that our method provides a less smoothing result with more natural textures (on window shutters and the rooftop), and less incorrect color blurring (red-colored above the sky in (a), (b), and (d)). Please zoom in to view the details.

first row of each presented image is JPEG compressed at quality factors from 10 to 40, with a step size of 10, and the second row is the recovered images via our model. As can be seen in Figure 7, while the significance of artifacts varies from the quality factors (e.g. see the sky region of "caps" and the background of "monarch"), our DCTransformer generates visually pleasing results with finer visual details.

To further distinguish our model from single-quality specified methods, we also explore its generalization capabilities at unseen quality factors set during training. Datasets of color LIVE1, Urban100, and BSDS500 images are used for such evaluation, with quality factors set from 10 to 80 and a step size of 5. As the result shown in Figure 8, our single model maintained great performance consistently even though the quality factor is at

that of more than one unseen value. We attribute it to the operation of quantization matrix embedding, since we do not extract features from the quantization matrix directly, but recover the original representation of coefficients in discrete cosine transformed value range by using a linear embedding. It can also be observed from the result in Figure 8 that the increase in PSNR is essentially consistent at low quality factors, and declines steeply as the quality factor reaches a higher value.

### 4.3 DCT Domain Evaluation

To analyze the performance of our model in the DCT domain, we adopt Jensen-Shannon divergence and Bhattacharyya distance as frequency quantitative evaluation metrics. These comparisons are conducted among DCT domain methods



Table 2: Pixel Domain Evaluation on **Grayscale** JPEG Images from Three Benchmark Datasets. Represented in **PSNR(dB)/SSIM/PSNR-B(dB)** Format. The Best and Second Best Performances are **Boldfaced** and **Underlined**, Respectively. Please Note that Marker ' Represents Quality Factor Specified Methods, and Marker \* Represents DCT Domain Methods.

Dataset	QF	JPEG	ARCNN'[11]	DnCNN-3[10]	MWCNN'[13]	DCSC[42]	RNAN'[43]
Classic-5	10	27.82/0.760/25.21	29.03/0.793/28.76	29.40/0.803/29.13	30.01/0.820/29.59	29.62/0.810/29.30	29.96/0.819/29.42
	20	30.12/0.834/27.50	31.15/0.852/30.59	31.63/0.861/31.19	32.16/0.870/31.52	31.81/0.864/31.34	32.11/0.869/31.26
	30	31.48/0.867/28.94	32.51/0.881/31.98	32.91/0.886/32.38	33.43/0.893/32.62	33.06/0.888/32.49	33.38/0.892/32.35
	40	32.43/0.885/29.92	33.32/0.895/32.79	33.77/0.900/33.23	34.27/0.906/33.35	33.87/0.902/33.30	34.27/0.906/33.40
LIVE1	10	27.77/0.773/25.33	28.96/0.808/28.68	29.19/0.812/28.90	29.69/0.825/29.32	29.34/0.818/29.01	29.63/0.824/29.13
	20	30.07/0.851/27.57	31.29/0.873/30.76	31.59/0.880/31.07	32.04/0.889/31.51	31.70/0.883/31.18	32.03/0.888/31.12
	30	31.41/0.885/28.92	32.67/0.904/32.14	32.98/0.909/32.34	33.45/0.915/32.80	33.07/0.911/32.43	33.45/0.915/32.22
	40	32.35/0.904/29.96	33.61/0.920/33.11	33.96/0.925/33.28	34.45/0.930/33.78	34.02/0.926/33.36	34.47/0.930/33.66
BSDS500	10	27.80/0.768/25.10	29.10/0.804/28.73	29.21/0.809/28.80	29.61/0.820/29.14	29.32/0.813/28.91	29.08/0.805/28.48
	20	30.05/0.849/27.22	31.28/0.870/30.55	31.53/0.878/30.79	31.92/0.885/31.15	31.63/0.880/30.92	31.25/0.875/30.27
	30	31.37/0.884/28.53	32.67/0.902/31.94	32.90/0.907/31.97	33.30/0.912/32.34	32.99/0.908/32.08	32.70/0.907/31.33
	40	32.30/0.903/29.49	33.55/0.918/32.78	33.85/0.923/32.80	34.27/0.928/33.19	33.92/0.924/32.92	33.47/0.923/32.27

Dataset	QF	FBCNN[15]	ARCRL[17]	Laplacian*[4]	FD-CRNet*[19]	QGAC*[14]	DCTransformer*
Classic-5	10	30.12/ <b>0.822</b> /29.80	<b>30.16/0.822/29.85</b>	28.04/0.763/25.44	29.54/0.806/29.14	29.84/0.812/29.43	30.12/ <b>0.822</b> /29.81
	20	32.31/ <u>0.872</u> /31.74	<b>32.37/0.873/31.84</b>	30.39/0.838/27.78	31.64/0.861/30.88	31.98/0.869/31.37	<u>32.33/0.872/31.81</u>
	30	33.54/ <u>0.894</u> /32.78	<b>33.60/0.895/32.89</b>	31.83/0.871/29.30	32.84/0.885/32.03	33.22/0.892/32.42	<u>33.55/0.894/32.84</u>
	40	34.35/ <u>0.907</u> /33.48	<b>34.43/0.908/33.58</b>	32.82/0.889/30.35	33.64/0.899/32.82	34.05/0.905/33.12	<u>34.37/0.907/33.53</u>
LIVE1	10	29.75/ <b>0.827</b> /29.40	<b>29.80/0.827/29.44</b>	27.98/0.777/25.81	29.24/0.813/28.88	29.51/0.825/29.13	29.76/ <b>0.827/29.44</b>
	20	32.13/0.889/31.57	<b>32.19/0.890/31.63</b>	30.31/0.856/28.09	31.52/0.880/30.73	31.83/0.888/31.25	<u>32.14/0.889/31.63</u>
	30	33.54/ <u>0.916</u> /32.83	<b>33.62/0.918/32.91</b>	31.67/0.890/29.43	32.84/0.908/31.96	33.20/0.914/32.47	<u>33.54/0.916/32.89</u>
	40	<u>34.53/0.931</u> /33.74	<b>34.62/0.931/33.84</b>	32.66/0.911/30.54	33.76/0.923/32.92	34.16/0.929/33.36	<u>34.52/0.931/33.79</u>
BSDS500	10	29.67/0.821/29.22	<b>29.70/0.822/29.27</b>	27.97/0.771/25.29	29.19/0.807/28.68	29.46/0.821/28.97	29.67/0.821/29.26
	20	32.00/ <u>0.885</u> /31.19	<b>32.06/0.886/31.27</b>	30.31/0.852/27.49	31.40/0.876/30.42	31.73/0.884/30.93	<u>32.01/0.885/31.27</u>
	30	33.37/ <u>0.913</u> /32.32	<b>33.45/0.914/32.41</b>	31.65/0.888/28.82	32.70/0.905/31.58	33.07/0.912/32.04	<u>33.38/0.913/32.40</u>
	40	<u>34.33/0.928</u> /33.10	<b>34.42/0.929/33.22</b>	32.62/0.909/29.83	33.59/0.921/32.42	34.01/0.927/32.81	<u>34.33/0.928/33.19</u>

since we directly compute the metrics from coefficients. For each frequency component  $c$  of the recovered DCT coefficients, we first compute the histogram of the coefficients into  $n$  bins, then normalize it to form a probability distribution  $P_c(i) = \{p_c(1), p_c(2), \dots, p_c(n)\}$  and  $Q_c(i) = \{q_c(1), q_c(2), \dots, q_c(n)\}$  to compute the metrics. All these indicators are computed on 64 frequencies separately and averaged as the distance between two DCT coefficients. Given the quantized DCT coefficients pairs  $X$  and  $Y$ , the Jensen-Shannon divergence between two probability distributions  $P$  and  $Q$  is defined as:

$$D_{JS}(X, Y) = \frac{1}{64} \sum_{c=1}^{64} \left( \frac{1}{2} D_{KL}(P_c \| M_c) + \frac{1}{2} D_{KL}(Q_c \| M_c) \right), \quad (17)$$

where  $D_{KL}$  represents the Kullback-Leibler divergence referring to [44],  $M_c$  is the average distribution of  $P_c$  and  $Q_c$ , and is defined as  $M_c = \frac{1}{2}(P_c + Q_c)$ .

The Bhattacharyya distance between two coefficients can be formulated as follows:

$$D_B(X, Y) = \frac{1}{64} \sum_{c=1}^{64} \left( -\log \left( \sum_{i=1}^n \sqrt{P_c(i)Q_c(i)} \right) \right), \quad (18)$$

where  $c$  goes from 1 to 64, denoting the frequency index; the  $P_c(i)$  and  $Q_c(i)$  are the probability distribution of the coefficients  $X$  and  $Y$ , respectively.

Table 3 reports the DCT domain evaluation result on the grayscale Classic-5 dataset at quality factors from 10 to 50. The smaller value indicates a more similar distribution to the lossless DCT coefficients and, correspondingly, higher-quality images can be reconstructed from these coefficients. Compared to QGAC, which is the state-of-the-art frequency domain method, our results have a significantly smaller JS divergence and Bhat-

Table 3: DCT Domain Evaluation of **JS Divergence / Bhattacharyya Distance** on Grayscale Classic-5 Dataset.

QF	JPEG		FD-CRNet		QGAC		Ours	
	JS ↓	Bha ↓	JS ↓	Bha ↓	JS ↓	Bha ↓	JS ↓	Bha ↓
10	0.2223	0.3589	0.0124	0.0134	0.0055	0.0060	<b>0.0044</b>	<b>0.0048</b>
20	0.2022	0.3228	0.0095	0.0101	0.0034	0.0036	<b>0.0022</b>	<b>0.0024</b>
30	0.1854	0.2900	0.0093	0.0099	0.0024	0.0025	<b>0.0017</b>	<b>0.0018</b>
40	0.1756	0.2713	0.0091	0.0096	0.0018	0.0019	<b>0.0013</b>	<b>0.0013</b>
50	0.1675	0.2577	0.0087	0.0093	0.0013	0.0014	<b>0.0009</b>	<b>0.0009</b>

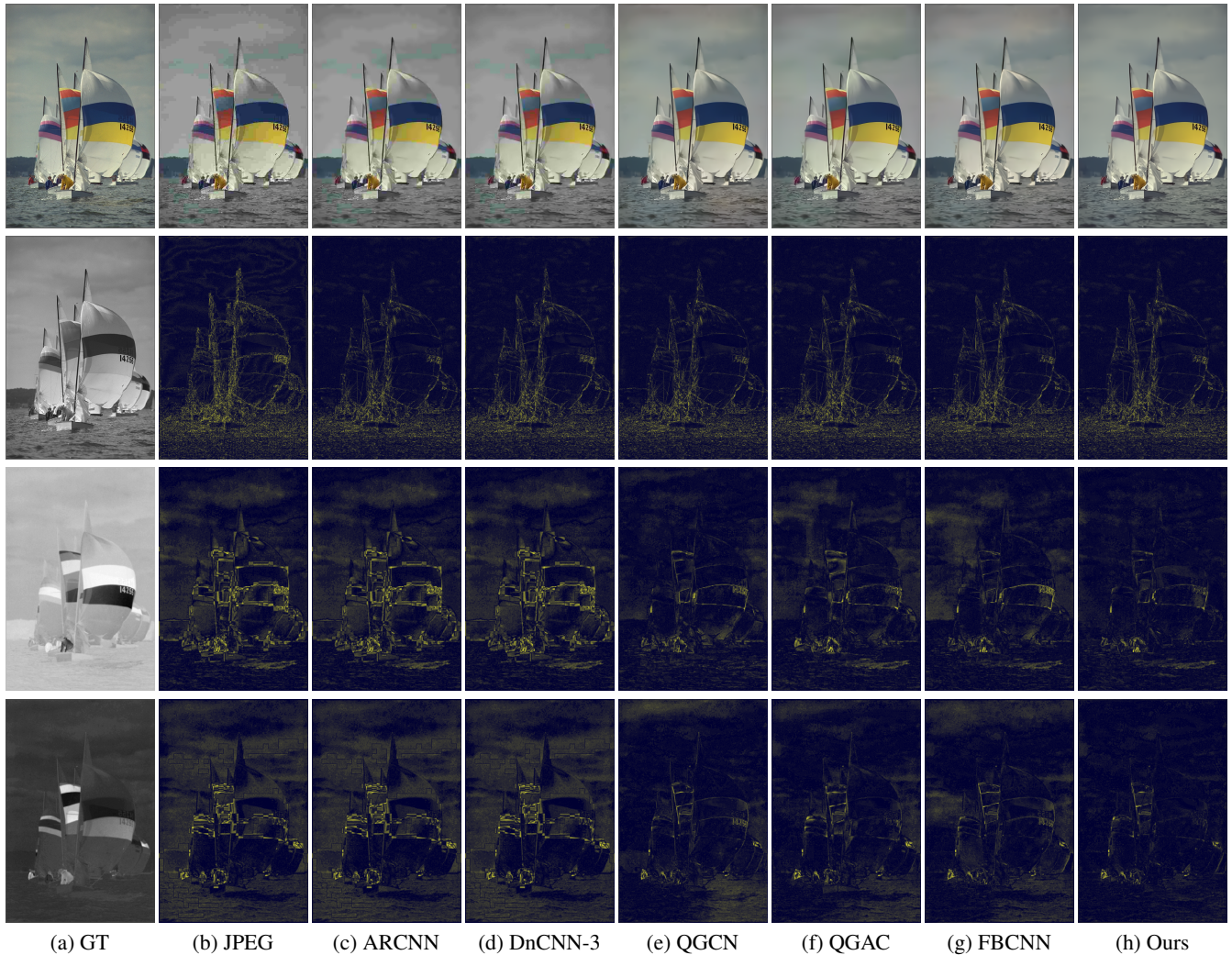


Figure 6: Channel residuals visualization on "LIVE1: sailing2.bmp" at the JPEG compression quality factor = 10. Each row (from top to bottom) represents the **color images**, **Y channels**, **Cb channels**, and **Cr channels**, respectively. The lighter place stands for a higher value of differences between the recovered images with ground truth. Note that although there are only slight differences in recovered Y channels, our DCTransformer performs significantly better on recovering color components (Cb and Cr), as shown in the last two rows with a darker result.

tacharya distance. The results indicate that our method achieves a better performance in recovering the quantized coefficients from the DCT domain perspective.

#### 4.4 Ablation Studies

We test a set of architectures of our model to investigate the contribution of each component. Our ablation models are trained exclusively on the DIV2k dataset ( $\approx 20\%$  of the training set) and for 50K iterations ( $\approx 10\%$  of the full training). We primarily investigate our model based on four aspects as below, while ensuring that the number of parameters remains approximately the same for fair comparisons. The results of the ablation analysis are presented in Table 4.

*a) The effectiveness of dual-branch architecture.* To verify whether the correlations between coefficients are modeled by our SFTB module, we explore three variations of the proposed

architecture. In the comparisons, parallel spatial branches and parallel frequential branches refer to two spatial or frequential breaches in parallel, replacing the original spatial-frequential branches. Successive branches imply the spatial and frequential branches are cascaded in succession. As shown in Table 4, the effectiveness of the dual-branch design is substantiated by the performance of our full-setting model.

*b) The effectiveness of feature fusion methods.* For the comparison of fusion methods, we utilize the adding operation between the output from two branches to replace the channel-wise feature concatenation. We also explore the contribution brought by the convolutional layer after the concatenation. The results are shown as "Add Fusion + Conv." and "Concat Fusion + No Conv." in Table 4. We can find that feature concatenation considerably improves the performance than adding operation, which fails to learn. It is worth noting that although only a small num-

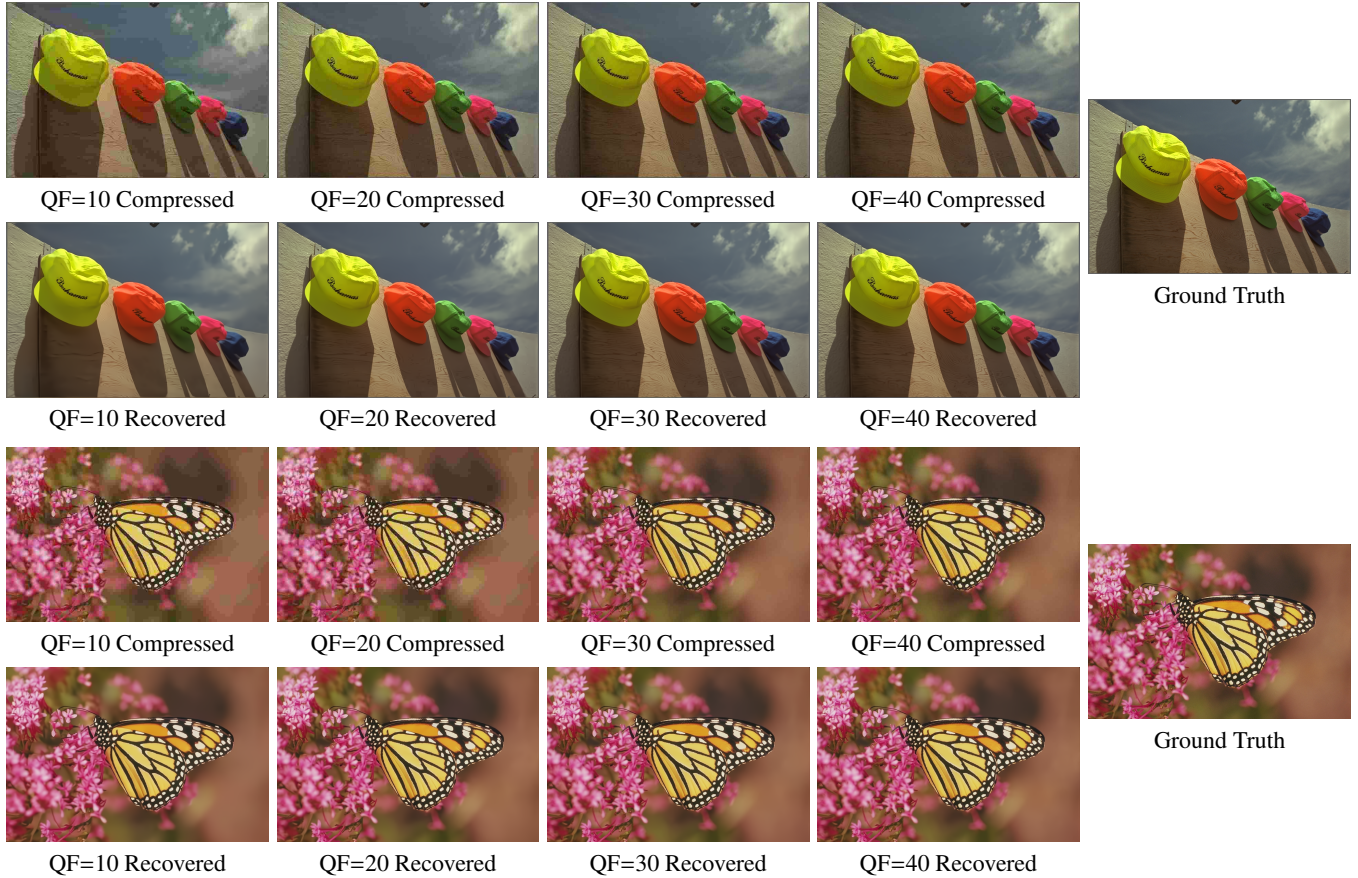


Figure 7: Examples of our single DCTransformer recover the compressed JPEG images of "LIVE1: caps.bmp" and "LIVE1: monarch.bmp" at different quality factors. Irrespective of the differences in input quality factors, all recovery results show consistency, which demonstrates the generalization capabilities of our model to cover a wide range of quality factors.

ber of parameters are reduced, the performance on PSNR drops significantly by up to 0.08 when the convolutional layer after the fusion operation is removed.

*c) The effectiveness of quantization matrix embedding.* We perform an ablation study on how the quantization matrix embedding contributes to our modeling. We first remove the quan-

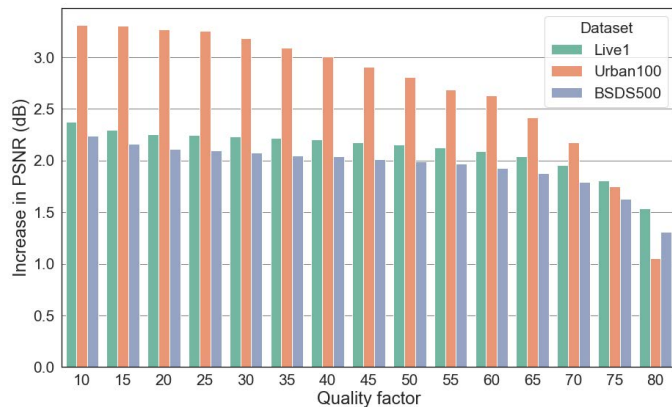


Figure 8: Generalization capabilities of our DCTransformer at quality factors from 10 to 80. Increase in PSNR of three color datasets LIVE1, Urban100, and BSDS500 is reported. At high quality factors, less information loss during the compression leads to a sharp drop in the PSNR increase.

Table 4: Ablation Analysis on Color LIVE1 Dataset. **PSNR(dB)/SSIM** is Reported and the Best Results are **Bold-faced**. Please Refer to Section IV-D for Detailed Settings of Each Model.

Comparison Methods	Params (M)	QF=20		QF=40	
		PSNR	SSIM	PSNR	SSIM
Parallel Spatial Branches	21.02	29.77	<b>0.864</b>	31.90	0.908
Parallel Frequential Branches	21.17	29.75	0.863	31.88	0.907
Successive Branches	19.87	29.58	0.856	31.65	0.900
Add Fusion + Conv.	21.09	29.73	0.861	30.85	0.905
Concat Fusion + No Conv.	19.87	29.75	0.862	31.89	0.907
Without Quantization Matrix	21.09	22.12	0.620	24.37	0.683
Concat Quantization Matrix	21.09	29.40	0.849	31.46	0.898
Standard Pixel Loss	21.09	29.76	0.863	31.86	0.907
Standard Frequency Loss	21.09	29.72	0.862	31.82	0.906
Full-Setting DCTransformer	21.09	<b>29.80</b>	<b>0.864</b>	<b>31.94</b>	<b>0.910</b>

tization matrix from our network, which finally leads the model to fail in recovery at any quality factors. Concatenate the quantization matrix with input coefficients is also tested. We suggest the proposed embedding helps handle different compression qualities, as the results reported in Table 4.

*d) The effectiveness of loss functions.* We adopt a common loss function in different domains to validate the effectiveness of our dual-domain loss. L1 is one of the most widely used losses in vision tasks, and we adopt it as the standard loss to train the same model for comparisons. We implement the L1 loss in pixel and frequency domains, to compute the loss within image pairs and DCT coefficient pairs, respectively. As shown in Table 4, the network trained with dual-domain loss (as "Full-setting DCTransformer") attains better performance than implementing any of the single-domain losses.

## 5 CONCLUSION

In this work, we present a novel DCT domain spatial-frequency Transformer (DCTransformer) for JPEG quantized coefficient recovery. Incorporating the quantization matrix embedding and luminance-chrominance alignment, our proposed DCTransformer has proven robustness in handling a wide range of quality factors and recovering the compressed luminance and chrominance components. As fully operating in the DCT domain, our single model is comparable to the state-of-the-art JPEG artifact removal methods on both pixel and frequency domain metrics. Extensive experiments also prove the effectiveness of our design. We suggest our model demonstrates the potential of DCT domain learning for JPEG artifact removal, which can possibly broaden the scope of image processing and computer vision fields.

## REFERENCES

- [1] Gregory K Wallace. The jpeg still picture compression standard. *Commun. ACM*, 34(4):30–44, 1991.
- [2] Nasir Ahmed, T\_ Natarajan, and Kamisetty R Rao. Discrete cosine transform. *IEEE Trans. Comput.*, 100(1): 90–93, 1974.
- [3] Albert J Ahumada and Rensheng Horng. Smoothing dct compression artifacts. In *Proc. SID*, volume 25, pages 708–708. Citeseer, 1994.
- [4] Jeffery R Price and Majid Rabbani. Biased reconstruction for jpeg decoding. *IEEE Sign. Process. Letters*, 6(12): 297–299, 1999.
- [5] Howard C Reeve III and Jae S Lim. Reduction of blocking effects in image coding. *Optical Engineering*, 23(1):34–37, 1984.
- [6] Peter List, Anthony Joch, Jani Lainema, Gisle Bjontegaard, and Marta Karczewicz. Adaptive deblocking filter. *IEEE Trans. Circuit Syst. Video Technol.*, 13(7):614–619, 2003.
- [7] Seok Bong Yoo, Kyuha Choi, and Jong Beom Ra. Post-processing for blocking artifact reduction based on inter-block correlation. *IEEE Trans. Multimedia*, 16(6):1536–1548, 2014. doi: 10.1109/TMM.2014.2327563.
- [8] Kostadin Dabov, Alessandro Foi, Vladimir Katkovnik, and Karen Egiazarian. Image denoising by sparse 3-d transform-domain collaborative filtering. *IEEE Trans. Image Process.*, 16(8):2080–2095, 2007.
- [9] Chao Dong, Chen Change Loy, Kaiming He, and Xiaoou Tang. Learning a deep convolutional network for image super-resolution. In *Proc. Eur. Conf. Comput. Vis., Zurich, Switzerland*, pages 184–199. Springer, 2014.
- [10] Kai Zhang, Wangmeng Zuo, Yunjin Chen, Deyu Meng, and Lei Zhang. Beyond a gaussian denoiser: Residual learning of deep CNN for image denoising. *IEEE Trans. Image Process.*, 26(7):3142–3155, 2017.
- [11] Pavel Svoboda, Michal Hradis, David Barina, and Pavel Zencik. Compression artifacts removal using convolutional neural networks. *arXiv preprint arXiv:1605.00366*, 2016.
- [12] Xiaoshuai Zhang, Wenhan Yang, Yueyu Hu, and Jiaying Liu. Dmncnn: Dual-domain multi-scale convolutional neural network for compression artifacts removal. In *Proc. IEEE Int. Conf. Image Process.*, pages 390–394. IEEE, 2018.
- [13] Pengju Liu, Hongzhi Zhang, Kai Zhang, Liang Lin, and Wangmeng Zuo. Multi-level wavelet-cnn for image restoration. In *Proc. IEEE Conf. Comput. Vis. Pattern Recog. Worksh.*, June 2018.
- [14] Max Ehrlich, Larry Davis, Ser-Nam Lim, and Abhinav Shrivastava. Quantization guided jpeg artifact correction. In *Proc. Eur. Conf. Comput. Vis., Glasgow, UK*, pages 293–309. Springer, 2020.
- [15] Jiayi Jiang, Kai Zhang, and Radu Timofte. Towards flexible blind jpeg artifacts removal. In *Proc. IEEE Int. Conf. Comput. Vis.*, pages 4997–5006, 2021.
- [16] Jianwei Li, Yongtao Wang, Haihua Xie, and Kai-Kuang Ma. Learning a single model with a wide range of quality factors for jpeg image artifacts removal. *IEEE Trans. Image Process.*, 29:8842–8854, 2020.
- [17] Xi Wang, Xueyang Fu, Yurui Zhu, and Zheng-Jun Zha. Jpeg artifacts removal via contrastive representation learning. In *Proc. Eur. Conf. Comput. Vis., Tel Aviv, Israel*, pages 615–631. Springer, 2022.
- [18] Jae Woong Soh and Nam Ik Cho. Variational deep image restoration. *IEEE Trans. Image Process.*, 31:4363–4376, 2022.
- [19] Tong Ouyang, Zhenzhong Chen, and Shan Liu. Towards quantized dct coefficients restoration for compressed images. In *IEEE Int. Conf. Vis. Commun. Image Process.*, pages 515–518. IEEE, 2020.
- [20] Ashish Vaswani, Noam Shazeer, Niki Parmar, Jakob Uszkoreit, Llion Jones, Aidan N Gomez, Łukasz Kaiser, and Illia Polosukhin. Attention is all you need. *Adv. Neural Inform. Process. Syst.*, 30, 2017.
- [21] Alexey Dosovitskiy, Lucas Beyer, Alexander Kolesnikov, Dirk Weissenborn, Xiaohua Zhai, Thomas Unterthiner, Mostafa Dehghani, Matthias Minderer, Georg Heigold, Sylvain Gelly, Jakob Uszkoreit, and Neil Houlsby. An image is worth 16x16 words: Transformers for image recognition at scale. *Int. Conf. Learn. Represent.*, 2021.

- [22] Ze Liu, Yutong Lin, Yue Cao, Han Hu, Yixuan Wei, Zheng Zhang, Stephen Lin, and Baining Guo. Swin transformer: Hierarchical vision transformer using shifted windows. In *Proc. IEEE Int. Conf. Comput. Vis.*, 2021.
- [23] Jingyun Liang, Jiezhong Cao, Guolei Sun, Kai Zhang, Luc Van Gool, and Radu Timofte. Swinir: Image restoration using swin transformer. *arXiv preprint arXiv:2108.10257*, 2021.
- [24] Charlie Nash, Jacob Menick, Sander Dieleman, and Peter Battaglia. Generating images with sparse representations. In *Proc. Int. Conf. Mach. Learn.*, pages 7958–7968. PMLR, 2021.
- [25] Jean-Baptiste Cordonnier, Andreas Loukas, and Martin Jaggi. On the relationship between self-attention and convolutional layers. *arXiv preprint arXiv:1911.03584*, 2019.
- [26] Kaiming He, Xiangyu Zhang, Shaoqing Ren, and Jian Sun. Deep residual learning for image recognition. In *Proc. IEEE Conf. Comput. Vis. Pattern Recog.*, June 2016.
- [27] Pierre Charbonnier, Laure Blanc-Feraud, Gilles Aubert, and Michel Barlaud. Two deterministic half-quadratic regularization algorithms for computed imaging. In *Proc. IEEE Int. Conf. Image Process.*, volume 2, pages 168–172. IEEE, 1994.
- [28] Eirikur Agustsson and Radu Timofte. Ntire 2017 challenge on single image super-resolution: Dataset and study. In *Proc. IEEE Conf. Comput. Vis. Pattern Recog. Worksh.*, pages 126–135, 2017.
- [29] Hamid R Sheikh, Muhammad F Sabir, and Alan C Bovik. A statistical evaluation of recent full reference image quality assessment algorithms. *IEEE Trans. Image Process.*, 15(11):3440–3451, 2006.
- [30] Hamid R. Sheikh and et al. LIVE image quality assessment database. <http://live.ece.utexas.edu/research/quality>, 2003.
- [31] Roman Zeyde, Michael Elad, and Matan Protter. On single image scale-up using sparse-representations. In *Curves and Surfaces: Int. Conf., Avignon, France*, pages 711–730, 2012.
- [32] Pablo Arbelaez, Michael Maire, Charless Fowlkes, and Jitendra Malik. Contour detection and hierarchical image segmentation. *IEEE Trans. Pattern Anal. Mach. Intell.*, 33(5):898–916, 2010.
- [33] Jia-Bin Huang, Abhishek Singh, and Narendra Ahuja. Single image super-resolution from transformed self-exemplars. In *Proc. IEEE Conf. Comput. Vis. Pattern Recog.*, pages 5197–5206, 2015.
- [34] Rawzor. Image compression benchmark. <http://imagecompression.info/>.
- [35] Diederik P. Kingma and Jimmy Ba. Adam: A method for stochastic optimization. In *Int. Conf. Learn. Represent.*, 2015.
- [36] Ilya Loshchilov and Frank Hutter. Sgdr: Stochastic gradient descent with warm restarts. In *Int. Conf. Learn. Represent.*, 2017.
- [37] Adam Paszke, Sam Gross, Francisco Massa, Adam Lerer, James Bradbury, Gregory Chanan, Trevor Killeen, Zeming Lin, Natalia Gimelshein, Luca Antiga, et al. Pytorch: An imperative style, high-performance deep learning library. *Adv. Neural Inform. Process. Syst.*, 32, 2019.
- [38] Gary Bradski. The opencv library. *Dr. Dobbs's Journal: Software Tools for the Professional Programmer*, 25(11): 120–123, 2000.
- [39] Independent JPEG Group et al. libjpeg: Independent jpeg group's software. <http://www.ijg.org/>, 1991.
- [40] Zhou Wang, Alan C Bovik, Hamid R Sheikh, and Eero P Simoncelli. Image quality assessment: from error visibility to structural similarity. *IEEE Trans. Image Process.*, 13(4): 600–612, 2004.
- [41] Changhoon Yim and Alan Conrad Bovik. Quality assessment of deblocked images. *IEEE Trans. Image Process.*, 20(1):88–98, 2010.
- [42] Xueyang Fu, Zheng-Jun Zha, Feng Wu, Xinghao Ding, and John Paisley. Jpeg artifacts reduction via deep convolutional sparse coding. In *Proc. IEEE Int. Conf. Comput. Vis.*, pages 2501–2510, 2019.
- [43] Yulun Zhang, Kunpeng Li, Kai Li, Bineng Zhong, and Yun Fu. Residual non-local attention networks for image restoration. In *Int. Conf. Learn. Represent.*, 2019.
- [44] Solomon Kullback and Richard A. Leibler. On information and sufficiency. *Ann. Math. Stat.*, 22(1):79–86, 1951. doi: 10.1214/aoms/1177729694.